Research Article

Nano Research
2020, 13(12): 3396–3402

ISSN 1998-0124 CN 11-5974/O4
https://doi.org/10.1007/s12274-020-3027-y

# Competing magnetic states in silicene and germanene 2D ferromagnets

Dmitry V. Averyanov[1], Ivan S. Sokolov[1], Mikhail S. Platunov[2,†], Fabrice Wilhelm[2], Andrei Rogalev[2], Pierluigi Gargiani[3], Manuel Valvidares[3], Nicolas Jaouen[4], Oleg E. Parfenov[1], Alexander N. Taldenkov[1], Igor A. Karateev[1], Andrey M. Tokmachev[1], and Vyacheslav G. Storchak[1] (✉)

[1] *National Research Center "Kurchatov Institute", Kurchatov Sq. 1, Moscow 123182, Russia*
[2] *ESRF-The European Synchrotron, CS 40220, 38043 Grenoble Cedex 9, France*
[3] *ALBA Synchrotron Light Source, Cerdanyola del Vallès, 08290 Barcelona, Spain*
[4] *Synchrotron SOLEIL, L'Orme des Merisiers, Gyf-sur-Yvette 91192, France*
[†] *Present address: Kirensky Institute of Physics, Federal Research Center KSC SB RAS, Akademgorodok 50, bld. 38, 660036 Krasnoyarsk, Russia*


**Received:** 16 June 2020 / **Revised:** 13 July 2020 / **Accepted:** 31 July 2020

## ABSTRACT

Two-dimensional (2D) magnets have recently developed into a class of stoichiometric materials with prospective applications in ultra-compact spintronics and quantum computing. Their functionality is particularly rich when different magnetic orders are competing in the same material. Metalloxenes $REX_2$ (RE = Eu, Gd; X = Si, Ge), silicene or germanene—heavy counterparts of graphene—coupled with a layer of rare-earth metals, evolve from three-dimensional (3D) antiferromagnets in multilayer structures to 2D ferromagnets in a few monolayers. This evolution, however, does not lead to fully saturated 2D ferromagnetism, pointing at a possibility of coexisting/ competing magnetic states. Here, $REX_2$ magnetism is explored with element-selective X-ray magnetic circular dichroism (XMCD). The measurements are carried out for $GdSi_2$, $EuSi_2$, $GdGe_2$, and $EuGe_2$ of different thicknesses down to 1 monolayer employing K absorption edges of Si and Ge as well as M and L edges of the rare-earths. They access the magnetic state in $REX_2$ and determine the seat of magnetism, orbital, and spin contributions to the magnetic moment. High-field measurements probe remnants of the bulk antiferromagnetism in 2D $REX_2$. The results provide a new platform for studies of complex magnetic structures in 2D materials.

## KEYWORDS

silicene, germanene, two-dimensional (2D) ferromagnetism, X-ray magnetic circular dichroism (XMCD), monolayer

## 1 Introduction

The discovery of intrinsic two-dimensional (2D) ferromagnetism (FM) in layered compounds brought to the monolayer (ML) limit [1, 2] has launched a burgeoning research field exploring the fundamental physics of magnetism in reduced dimensions, emerging quantum phases, potential development of new spin-related devices, and applications [3–5]. The material landscape of 2D ferromagnets is shaped by atomically thin crystals built upon transition metal magnetic ions Cr [1, 2], V [6, 7], Mn [8], and Fe [9, 10] as well as rare earths (REs) [11, 12]. Intrinsic 2D magnetic materials are highly amenable to external stimuli [3, 4]. Thus, 2D FM is particularly appealing once borders or coexists with other magnetic orders, an example being antiferromagnetism (AFM) in the 2D ferromagnet $CrI_3$ established with magneto-optical Kerr effect microscopy [2], second-harmonic generation [13], single-spin microscopy [14], and magnetic force microscopy [15]. In particular, 2D magnetic states can be controlled by gating [16], electrostatic doping [17] or pressure tuning of layer stacking [18]. Magnetic-field-induced AFM-to-FM transitions are responsible for giant tunneling magnetoresistance in spin-filter van der Waals heterostructures [19].

A competition between FM and AFM orders is inherent in magnetic metalloxenes [11, 12], a class of materials based on 2D-Xenes silicene and germanene [20, 21]. These elemental analogues of graphene are promising candidates for nano-electronics [22] and spintronic applications [23, 24]; in particular, they support regular lattices of magnetic ions, such as REs $Eu^{2+}$ and $Gd^{3+}$. Silicene-based $EuSi_2$ and $GdSi_2$ [11] as well as germanene-based $EuGe_2$ and $GdGe_2$ [12] are intrinsic 2D ferromagnets exhibiting in-plane magnetism. Strong thermal fluctuations in the $REX_2$ (X = Si or Ge) metalloxenes (dubbed REXenes) are suppressed by a field-induced anisotropy to open up a spin-wave excitation gap, as witnessed by a pronounced dependence of the transition temperature on weak magnetic fields [11, 12], similar to that in $Cr_2Ge_2Te_6$ [1]. Thickness dependence of the magnetic order in REXenes is particularly striking: Multilayer (bulk) $REX_2$ are 3D antiferromagnets [25, 26] whereas a few monolayer (ML) materials exhibit 2D FM [11, 12] (hematene [9] and $V_5Se_8$ [7] are other 2D ferromagnets derived from AFM parent compounds). Naturally, the AFM-to-FM evolution goes through a stage where both magnetic orders coexist, manifested experimentally by exchange bias in magnetization [12]. The changes in the magnetic state of

Address correspondence to mussr@triumf.ca

2D REXenes accompany profound transformations of the electronic structure: The observed laws of electron transport in a few MLs $RESi_2$ are essentially layer-dependent, ranging from a Kondo metal (4 ML) to a spin-gap insulator at 1 ML exhibiting colossal negative magnetoresistance [27].

The REXene materials hold promise for applications in reprogrammable spin logic and nonvolatile memory [28], $EuGe_2$ electron transport exhibits a high carrier mobility and bears marks of a topologically non-trivial state [26]. In modern electronics, a significant advantage of $REX_2$ is their natural integration with silicon/germanium technological platforms. However, this feature makes an obstacle in studying 2D magnetism: The FM of REXene monolayers is established employing SQUID magnetometry [11, 12]. The integration with a Si or Ge substrate restricts measurements to rather low magnetic fields—in high fields, the diamagnetic signal from the substrate dominates, making a magnetic signal from $REX_2$ difficult to extract. This limitation can be overcome by high-field techniques having an advantage to be surface-sensitive and element-selective. These techniques may shed light on still outstanding questions. First, an independent confirmation of the magnetic state in 2D REXenes is worthwhile; its importance is highlighted by the controversy of monolayer $VSe_2$, which is reported as a room-temperature 2D ferromagnet based on magnetization measurements [6] whereas X-ray magnetic circular dichroism (XMCD) studies find no signatures of magnetism [29, 30]. Second, the FM moments (per formula unit) in REXenes are significantly smaller than those expected from half-filled 4f shells of $Eu^{2+}$ and $Gd^{3+}$ ions. It is important to determine the seat of magnetism, i.e., whether it is confined to the RE ions or the 2D-Xenes are also spin-polarized. On the other hand, the smallness of the FM moments may indicate an admixture of non-trivial electronic configurations to the half-filled 4f shells of the RE ions leading to sizable orbital moments. The reduced FM signal in REXenes (in comparison with other FM compounds of Eu [31] and Gd [32]) makes us wonder about the remaining moments, non-FM orders or frustration, the possibilities of concurrent paramagnetism or remnants of the bulk AFM state. In order to unravel the nature of these states, measurements in high magnetic fields would be instrumental.

Here, we produce a series of REXenes—$EuSi_2$, $GdSi_2$, $EuGe_2$, $GdGe_2$—with thicknesses ranging from 1 to 4 ML and explore their magnetic states by element-selective XMCD measurements at the $M_{4,5}$ edges of Gd, $L_3$ edge of Gd and Eu as well as at the K edge of Si and Ge. We study XMCD signals in high magnetic fields to provide experimental answers to the questions posed above concerning the presence, seat, and nature of magnetism in REXenes.

## 2 Results and discussion

### 2.1 Synthesis and characterization of REXenes

2D films of $REX_2$ are synthesized employing reactive molecular beam epitaxy (MBE). The technique allows for layer-by-layer synthesis with kinetic control over the process. Synthesis proceeds via a direct reaction between RE atoms and the X substrate:

$$RE + 2X = REX_2 \quad (1)$$

We employ Si(111) and Ge(111) substrates whose surfaces are in fact covalently bound silicene and germanene layers, respectively. Thus, the substrate is both a reactant and a platform stabilizing the required polymorph of $REX_2$ and its orientation, driven by the lattice match of the Xene layers at the $REX_2$/X(111) interface. The synthesis conditions—the substrate temperature, RE flow and deposition time, and annealing temperature and time—are optimized for each REXene $EuSi_2$, $GdSi_2$, $EuGe_2$, and $GdGe_2$, as reported in Refs. [11, 12]. Structures of different thicknesses set by duration of the RE deposition, ranging from 1 to 4 ML, have been produced.

The structural characterization of the samples starts in the MBE growth chamber. Reflection high-energy electron diffraction (RHEED) controls the surface morphology and determines the lateral lattice parameters of the films. Figure 1(a) presents a typical RHEED image taking 4 ML $GdSi_2$ as an example; streaks are well-developed and bright. Samples are further studied *ex situ*. X-ray diffraction (XRD) provides integral characterization of the films. The fundamental limitations of the technique and the XRD spectrometer make the study useful for samples thicker than 2 ML. A $\theta$–$2\theta$ XRD scan for 4 ML $GdSi_2$ (Fig. 1(b)) illustrates the absence of side products and alternative orientations of the layered structure—a property common to all synthesized REXene samples. Scanning transmission electron microscopy (STEM) has been used to determine the microstructure of the films and verify their thicknesses. High-angle annular dark-field imaging (HAADF) of REXene cross-sections reveals rows of RE atoms (bright spots) parallel to the substrate surface (see Fig. 1(d) for a typical image of 4 ML $GdSi_2$, silicene layers are not resolved because of the Z-contrast). Typical HAADF images of thinner films can be found in Refs. [11, 12, 27]. It is worth noting that Gd-based REXenes thicker than 1 ML are likely to contain flat Xene layers, prone to a significant number of vacancies [33].

All these techniques evidence a superb structural quality of the samples. This is an important prerequisite for any subsequent magnetic measurements: For example, monolayer $VSe_2$ provides a case where the same technique may show 2D magnetism [34] or no magnetism at all [29, 30], the difference being attributed to the quality of the samples [34]. SQUID magnetization measurements of all REXene samples demonstrate 2D FM in accordance with the data on the saturation moments, magnetization anisotropy, effective Curie temperatures, and their dependence on weak magnetic fields, reported in Refs. [11, 12]. This dependence is illustrated by the example of 4 ML $GdSi_2$ (Fig. 1(c)) to show a profound evolution of magnetization curves as the in-plane magnetic field changes from 2–3 to 1,000 Oe—a fingerprint of 2D ferromagnetism.

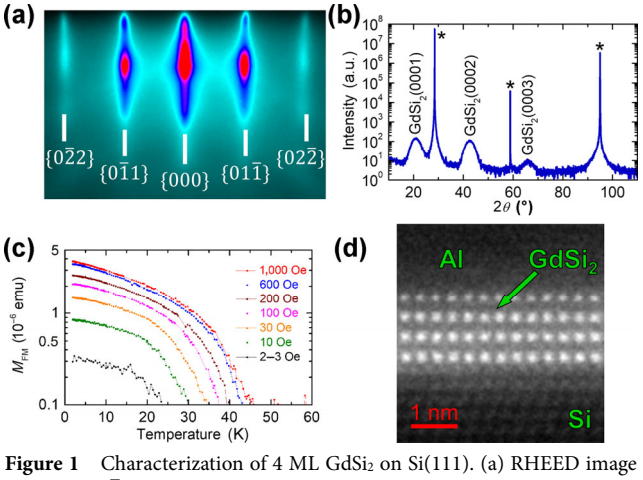


**Figure 1** Characterization of 4 ML $GdSi_2$ on Si(111). (a) RHEED image along the [1$\bar{1}$0] azimuth of the Si substrate. (b) $\theta$–$2\theta$ XRD scan; asterisk denotes peaks from the substrate. (c) Temperature dependence of the FM moment in in-plane magnetic fields 2–3 (black), 10 (green), 30 (orange), 100 (magenta), 200 (maroon), 600 (blue), and 1,000 Oe (red). (d) HAADF-STEM cross-sectional image viewed along the [1$\bar{1}$0] zone axis of the Si substrate.

## 2.2 XMCD of REXenes

SQUID magnetization measurements, enabled by large areal sizes of the REXene materials, require complementary studies by other techniques. Typically, research on 2D magnetic materials relies on optical and electrical methods [35]. A link between magnetism and electron transport in REXenes has already been demonstrated [11, 12, 27]; in contrast, optical experiments are lacking. In studies of 2D magnetism, the most commonly used magneto-optic effects are magnetic circular birefringence and dichroism [35]. We give preference to XMCD because of its element and shell selectivity. XMCD has proven useful in studies of layered magnetic materials $VSe_2$ [29, 30, 34], $CrI_3$ [36], $Fe_3GeTe_2$ [37, 38], and supramolecular lattices [39]. As for RE-based 2D materials, XMCD has been employed to detect emerging 2D ferromagnetism at the surface of valence-fluctuating $EuIr_2Si_2$ [40].

First, we attempted to study the magnetic response of Xene layers in REXenes. To this purpose, we employed 4 ML $GdSi_2$ and 1 ML $EuGe_2$—the REXenes with the highest FM moment per film surface area unit [11, 12]. Figure 2 presents X-ray absorption spectroscopy (XAS) and XMCD spectra in these materials at the K absorption edges of Si and Ge, respectively. An important problem of such measurements is the presence of the substrate diluting the XMCD to XAS ratio; also, XMCD at K edges is expected to be more sensitive to the orbital rather than spin moment [41]. The XMCD signals are rather small but apparently above the detection/noise level. A quantitative analysis here would be rather difficult because we cannot differentiate the XAS signals coming from the film and the substrate. However, theoretical calculations of RE functionalized silicene [42] predict tiny magnetic moments on Si, on the order $10^{-2}$ – $10^{-3}$ $\mu_B$; the Si K signal in $GdSi_2$ is comparable to that in $Fe_3Si$, a non-layered ferromagnet [43]; the Ge K XMCD signal in $EuGe_2$ is much lower than that in other FM Ge-based compounds [44]. Both Si K and Ge K XMCD signals in the REXenes have similar spectral shapes and the same sign which indicates that the p states (probed at the K edge) are spin-polarized in a similar manner. It may well be that the role of Xenes in 2D magnetism of REXenes is rather indirect, although they are essential components as revealed by a fundamental difference in the magnetic states of tetragonal and hexagonal $GdSi_2$ polymorphs [11].

For a more robust probe of REXene magnetism, we turn our attention to element-selective XMCD for RE ions. Figure 3(a) shows XAS and XMCD spectra for the $M_{4,5}$ absorption edges (3d → 4f shell transition) of Gd in 4 ML $GdSi_2$, measured at the BOREAS beamline. First, we notice that the XMCD signals are rather large. This is not a trivial result taking into account that in the $VSe_2$ 2D magnet [6], the measured XMCD signals at V $L_{2,3}$ are below the detection sensitivity of the synchro-

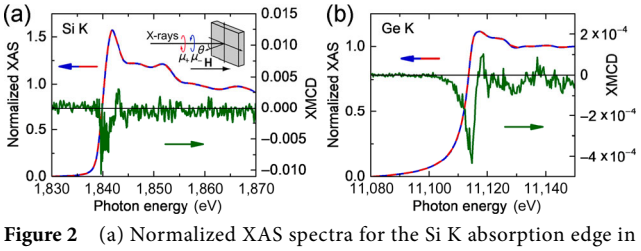


**Figure 2** (a) Normalized XAS spectra for the Si K absorption edge in 4 ML $GdSi_2$ in a magnetic field of 6 T at 20 K: right (red) and left (blue) circular polarizations; their difference (green) makes a normalized XMCD signal. Inset sketches the experimental setup. (b) Normalized XAS spectra for the Ge K absorption edge in 1 ML $EuGe_2$ in a magnetic field of 17 T at 3 K: right (red) and left (blue) circular polarizations; their difference (green) makes a normalized XMCD signal.

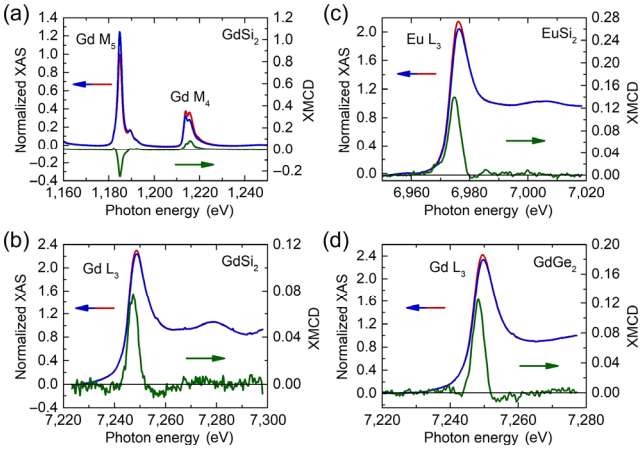


**Figure 3** Normalized XAS spectra: right (red) and left (blue) circular polarizations; their difference (green) makes a normalized XMCD signal. (a) Gd $M_4$ and Gd $M_5$ absorption edges in 4 ML $GdSi_2$ in a magnetic field of 6 T at 20 K. (b) Gd $L_3$ absorption edge in 4 ML $GdSi_2$ in a magnetic field of 17 T at 3 K. (c) Eu $L_3$ absorption edge in 1 ML $EuSi_2$ in a magnetic field of 17 T at 3 K. (d) Gd $L_3$ absorption edge in 1 ML $GdGe_2$ in a magnetic field of 17 T at 3 K.

tron facilities [29, 30]. On the other hand, the XMCD spectra establish RE layers as a seat of magnetism in 2D REXenes. This result is confirmed by independent studies of the Si K and Gd $M_{4,5}$ absorption edges in 4 ML $GdSi_2$ at the DEIMOS beamline of the SOLEIL synchrotron light source (not shown).

The ground state expectation values of the spin $\langle S_z \rangle$ and orbital $\langle L_z \rangle$ moments of the Gd ion have been calculated using the corresponding XMCD sum rules [45, 46]. In the case of the $M_{4,5}$ absorption edge, they read

$$\langle L_z \rangle = 2\frac{q}{r}N_H \text{ and } \langle S_{eff} \rangle = \langle S_z \rangle + 3\langle T_z \rangle = \frac{5p-3q}{2r}N_H \quad (2)$$

where $p$ is the integral of the XMCD intensity at the $M_5$ edge, $q$ is the integral of the XMCD intensity at both $M_4$ and $M_5$ edges, $r$ is the integral of the XAS intensity after an atomic step-function subtraction, and $N_H$ is the number of holes in the 4f shell. According to electron energy loss spectra of $GdSi_2$ [11], the metal atoms are in the Gd(III) valence state; therefore, we can assume that the number of 4f holes $N_H$ is equal to 7. The term $\langle T_z \rangle$, the expectation value of the intra-atomic magnetic dipole operator, can be large for 4f elements; for $Gd^{3+}$ ions, however, it is rather small [47] and can therefore be neglected ($\langle S_z \rangle \cong \langle S_{eff} \rangle$).

Application of these rules to the XMCD spectra of $GdSi_2$ at the $M_{4,5}$ absorption edges produces $\langle L_z \rangle = -0.1$ and $\langle S_z \rangle = -1.5$. First, we can see that the total magnetic moment $m_z = 3.1\ \mu_B$ is several times higher than the estimate of the FM moment (0.6 $\mu_B$ at 0.1 T) from low-field SQUID measurements in the same $GdSi_2$ film [11]; however, the XMCD magnetic moment is still far from the theoretical saturation moment of 7$\mu_B$ for $4f^7$ Gd ion (according to Hund's rule of maximum multiplicity). The electronic configuration of $Gd^{3+}$ ions, $^8S_{7/2}$ ($4f^7$), points at a spin magnetism with a vanishing orbital moment, it is also observed in XMCD studies of Gd-based magnetic compounds [48]. Simple density functional theory (DFT) generalized gradient approximation (GGA) calculations of Gd-adsorbed silicene do not reproduce the smallness of the orbital moment in $GdSi_2$; however, on-site Coulomb repulsion strongly suppresses the orbital moments [42].

To explore saturation of the magnetic moments, high magnetic fields and low temperatures are instrumental. Therefore, we complement XMCD at the $M_{4,5}$ absorption

edges of Gd ions in $GdSi_2$ by a study of the Gd $L_3$ absorption edge at high magnetic fields (up to 17 T) provided by the European Synchrotron Radiation Facility (ESRF) facilities—it corresponds to 2p → 5d shell transition and probes the magnetic ordering mediated by the polarized 5d band. In this case, however, separation of spin and orbital contributions becomes unfeasible. XMCD at the $L_3$ absorption edges of Gd and Eu has proven useful in the magnetic structure determination [49, 50]. Figure 3(b) shows XAS and XMCD spectra at the Gd $L_3$ edge in 4 ML $GdSi_2$. A noticeable XMCD signal is detected attesting the capability of this technique in the hard X-ray range to probe the REXene magnetism in the limit of ML thickness—this constitutes a remarkable achievement as the corresponding attenuation length exceeds that of the soft X-ray range (commonly used for studies of 2D materials) by 3 orders of magnitude. The same is true for other REXenes. In particular, $EuSi_2$ (Gd replaced by Eu) demonstrates an XMCD signal (Fig. 3(c)) similar to that in $GdSi_2$. The same applies to the Gd $L_3$ XMCD signal in $GdGe_2$ (silicene replaced by germanene, Fig. 3(d)). However, the comparison is more meaningful when dependences of the XMCD signal on magnetic field and temperature are probed.

These element selective magnetization data are presented in Fig. 4 for a number of materials. Their rationalization is not trivial: How to fit the field and temperature dependence of the XMCD signal for a 2D ferromagnet emerging from an AFM state is an open question. We employ a simplified fit of high-field data by a sum of a saturated ferromagnetic contribution $M_{FM}$ and a modified Brillouin function [51]:

$$M(H,T) = M_{FM}\mathrm{sgn}(H) + (M_S - M_{FM})B_J(x) \quad (3)$$

where $x = \dfrac{Jg\mu_B H}{k_B(T-\theta)}$, $B_J$ is the standard Brillouin function, $J$ (= 7/2) is the total electron angular momentum, $g$ (= 2) is the Lande $g$-factor, $\mu_B$ is the Bohr magneton, $k_B$ is the Boltzmann constant, and $\theta$ is the Weiss constant whose positive or negative values correspond to FM or AFM interaction, respectively. For each sample, $M_S$, the saturation magnetization, is a global parameter whereas $M_{FM}$ and $\theta$ are considered $T$-dependent.

Magnetic field dependence of the Eu magnetic moment (derived from XMCD signals normalized to the theoretical high-field limit) in 1 ML $EuSi_2$ (Fig. 4(a)) shows some characteristic features. The low-temperature ferromagnetic contribution $M_{FM}$ is close to the estimate based on SQUID measurements [11]. The value of $M_{FM}$ approaches zero as temperature increases. A higher temperature diminishes the magnetic moment and

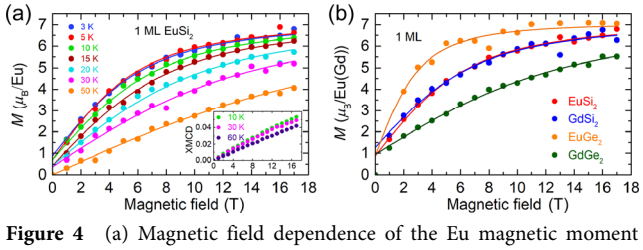


**Figure 4** (a) Magnetic field dependence of the Eu magnetic moment (derived from the Eu $L_3$ XMCD signal) in 1 ML $EuSi_2$ at 3 (blue), 5 (red), 10 (green), 15 (maroon), 20 (cyan), 30 (magenta), and 50 K (orange); fits to Eq. (3) are shown as continuous lines. The data and fits are scaled uniformly to $M_S = 7\mu_B$/Eu(Gd). Inset provides magnetic field dependence of XMCD signals for the Eu $L_3$ absorption edge in 14 ML $EuSi_2$ at 10 (green), 30 (magenta), and 60 K (blue). (b) Magnetic field dependence of the RE magnetic moment calculated from the Eu $L_3$ and Gd $L_3$ XMCD signals in 1 ML $EuSi_2$ (red), 1 ML $GdSi_2$ (blue), 1 ML $EuGe_2$ (orange), and 1 ML $GdGe_2$ (green); all at 3 K, fits to Eq. (3) are also shown.

makes the $M(H)$ dependence almost linear. A similar effect is brought by film thickness: XMCD signals of a 14 ML sample of $EuSi_2$ (at this thickness, 2D FM is suppressed) demonstrate a linear dependence on the magnetic field (inset in Fig. 4(a)). It is instructive to compare XMCD data for all 4 REXenes of the same thickness 1 ML (Fig. 4(b)). The overall behaviour correlates with the SQUID data [11, 12]: Below saturation, $GdSi_2$ and $EuSi_2$ exhibit close values of magnetization; it is lower in $GdGe_2$ and higher in $EuGe_2$. However, the fits fail to differentiate between the FM contributions in the 4 REXenes. We would like to stress that although the fits are quite reasonable numerically, their interpretation may well miss some salient features of XMCD in REXenes. The theoretical treatment of 2D magnetism for non-bipartite lattices, such as the triangular lattice of REXenes, is severely complicated by potential coexistence of several ordered structures at a given temperature [52].

The parameter $\theta$ in Eq. (3) gives an effective measure of magnetic correlations in the material placed in high magnetic fields when the FM is saturated. Figure 5 illustrates the evolution of $\theta$ with temperature and sample thickness in 2D $EuSi_2$. First, we notice that $\theta$ is always negative, i.e., corresponds to antiferromagnetic correlations coexisting with the saturated 2D FM. The correlations diminish with temperature. Most importantly, the parameter $\theta$ decreases as the sample approaches the 1 ML limit, although does not vanish altogether – even 1 ML samples carry some remnants of the bulk AFM. The evolution is gradual, in contrast to $NiPS_3$ whose AFM order persists down to 2 ML but is suppressed in the 1 ML limit [53]. Behaviour of other REXenes is similar to that of $EuSi_2$: at 3 K, $\theta$ changes from –36.0 K in 4 ML to –13.8 K in 1 ML $GdSi_2$, from –40 K in 4 ML to –4.5 K in 1 ML $EuGe_2$, and from –36.5 K in 4 ML to –27.7 K in 1 ML $GdGe_2$. It is noteworthy that the value of $\theta$ in 1 ML REXenes correlates with their 2D FM: a smaller value of $\theta$ (weaker AFM correlations) accompanies a higher value of the 2D FM signal in SQUID measurements [11, 12].

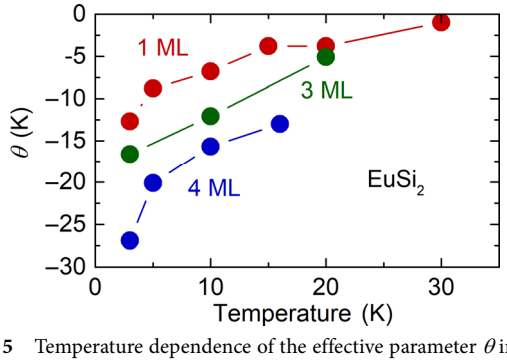


**Figure 5** Temperature dependence of the effective parameter $\theta$ in fits of XMCD data to Eq. (3) for 1 ML $EuSi_2$ (red), 3 ML $EuSi_2$ (green), and 4 ML $EuSi_2$ (blue).

## 3 Conclusions

2D magnetism in layered materials is a relatively new field of research. Significant efforts are invested in studies of 2D magnetic materials and their magnetic structures but a lot are yet to be done and understood, especially in systems with competing magnetic orders. Here, we studied high-field magnetic responses of 2D REXenes. Significant advantages of this research is that (i) REXenes form a class of 2D ferromagnets, i.e., we have been able to study 4 different compounds; (ii) they exhibit a thickness-dependent AFM-to-FM evolution. In the present study, we confirmed independently the magnetic state in REXenes, determined the seat of magnetism, orbital,

and spin contributions to the magnetic moment, mapped high-field XMCD data, and detected correlations between the FM and AFM. The study of REXenes coupled with a substrate is enabled by the element selectivity and surface sensitivity of XMCD – free-standing REXenes are yet to be produced although mechanical exfoliation of metalloxenes has recently been demonstrated [54]. Further research in this direction can be envisioned. It would be interesting to explore the changes in the magnetic states of REXenes arising from nanopatterning which can be brought about for example by their growth on vicinal X(111) substrates [55]. On the other hand, the discovery of 2D ferromagnetism in Eu/graphene bilayer ($EuC_6$ monolayer) [56] suggests its XMCD study, to compare with Eu-based REXenes.

## 4 Experimental section

### 4.1 Synthesis

The films of REXenes are synthesized in the Riber Compact 12 system for molecular beam epitaxy. Base pressure in the vacuum chamber does not exceed $10^{-10}$ Torr. The substrate temperature is monitored with PhotriX ML-AAPX/090 infrared pyrometer operating at a 0.9 μm wavelength whereas the effusion cell temperatures are measured with thermocouples. The molecular flux intensities are determined with a Bayard-Alpert ionization gauge placed in the position of the substrate. The substrates employed are 1 inch × 1 inch wafers of single-crystalline Si(111) and Ge(111) with miscut angles less than 0.5°. The substrates are prepared for REXene synthesis by removal of the native oxide from their surfaces, brought about by heating up to 950 (Si) and 650 °C (Ge).

Synthesis of ultrathin $GdSi_2$ films is carried out by heating the Si(111) substrate to 420 °C and its exposure to a $10^{-8}$ Torr flux of 4N Gd evaporated from a Knudsen cell effusion source heated to 1,210 °C. Synthesis of $EuSi_2$ requires a different procedure to stabilize the silicene-based polymorph. A Eu film is deposited on the Si(111) substrate at room temperature employing a $1.5 \times 10^{-8}$ Torr flux of 4N Eu from an effusion cell heated to 400 °C. Then, the film is annealed for 5 min at 340 °C to accomplish the reaction between the Eu layer and the Si(111) substrate. $GdGe_2$ and $EuGe_2$ are synthesized employing the same fluxes of Gd and Eu; RE metals are deposited on the Ge(111) substrate at 400 and 290 °C, respectively. $EuGe_2$ films are annealed for half an hour at 500 °C. All the REXene films are capped at room temperature with a 20 nm layer of either amorphous $SiO_x$ or polycrystalline 5N Al, to prevent degradation from air exposure.

### 4.2 Characterization

Structural properties of the films are studied with a combination of *in situ* and *ex situ* techniques. In the growth chamber, the crystal quality and the surface morphology of the films are monitored with an RHEED diffractometer furnished with the kSA 400 Analytical RHEED System. X-ray diffraction scans are measured *ex situ* employing the Rigaku SmartLab 9 kW diffractometer operating at a 1.54056 Å wavelength. The atomic structure of the films is studied further with high-resolution electron microscopy. Cross-sectional lamellae are prepared in the Helios NanoLab 600i scanning electron microscope/focused ion beam (FIB) dual beam system. The following procedures are carried out: deposition of a 2 μm protective Pt layer; shaping of the lamellae to dimensions 2 μm × 5 μm × 5 μm employing FIB with 30 keV $Ga^+$ ions; further thinning and cleaning of the lamellae with 5 and 2 keV $Ga^+$ ions, respectively. The specimens are then transferred to the TEM/STEM Titan 80-300 Cs-corrected microscope and the microstructure of the films is studied in the HAADF mode.

Low-field magnetic properties of the films are determined with MPMS XL-7 SQUID magnetometer employing the reciprocating sample option. The samples are mounted in plastic straws and oriented with respect to external magnetic field with accuracy better than 2°. Magnetic signals from a few MLs of REXene are small – their extraction requires the substrate diamagnetism to be accounted for. We tried two approaches: (i) subtraction of the substrate magnetic signal measured in a separate experiment; (ii) subtraction of all magnetic signals scaling linearly with magnetic field. This second approach requires magnetic measurements in a high magnetic field $H'$ – the small ferromagnetic signal is assumed to be saturated and surpassed by other contributions. The ferromagnetic moment is then evaluated as

$$M_{FM}(H) = M(H) - M(H')\frac{H}{H'} \quad (4)$$

Both approaches provide similar results certifying the consistency of the ferromagnetic moment estimates.

### 4.3 XAS and XMCD studies

Complementary XAS and XMCD measurements are carried out at 3 beamlines operating at different X-ray energy ranges: (i) The Eu $L_3$, Gd $L_3$, and Ge K absorption edges are studied at the ESRF ID12 beamline in magnetic fields up to 17 T. Circularly polarized radiation is generated by a helical undulator APPLE-II. The polarization rate after monochromator exceeds 92% at the Eu $L_3$ and Gd $L_3$ edges and close to 95% at the Ge K absorption edge. The spectra are recorded in the total fluorescence yield detection mode in a backscattering geometry. (ii) The Gd $M_{4,5}$ and Si K absorption edges are studied at the BOREAS beamline of the ALBA synchrotron light source [57] in magnetic fields up to 6 T. X-ray beam is also produced by an APPLE-II undulator operating on the 3rd harmonic at 90% circular polarization. The spectra are measured in the total electron yield (TEY) mode. (iii) Another set of experiments at the Gd $M_{4,5}$ and Si K absorption edges is carried out at the DEIMOS beamline of the SOLEIL synchrotron light source [58] in magnetic fields up to 6 T. X-ray beam is produced by an APPLE-II undulator operating on the 2nd harmonic at 98% circular polarization. The spectra are measured in the TEY detection mode.

The samples are glued to a cold finger with GE Varnish to ensure a thermal contact. Magnetic field is generated along the incident X-ray beam by superconducting cryomagnets. The angle between the sample basal plane and the applied magnetic field is 10° at the ESRF beamline ID12 (for experiments at the Ge K edge, this angle was tuned to be as small as possible), 15° or 90° in BOREAS experiments and 90° in SOLEIL. XMCD signals, proportional to the sample magnetization component along the beam, are collected as the difference between XAS spectra with right and left helicities of the incident X-ray beam. To establish the absence of experimental artefacts, XMCD measurements are repeated for the opposite direction of the applied magnetic field.

## Acknowledgements

This work was supported by National Research Center (NRC) "Kurchatov Institute" (No. 1359, characterization) and the Russian Science Foundation (No. 19-19-00009 (synthesis) and No. 20-79-10028 (magnetization measurements)). D. V. A. also acknowledges support from the President's scholarship (SP 1398.2019.5). The measurements have been carried out using

equipment of the resource centers of electrophysical and electron microscopy techniques in NRC "Kurchatov Institute".

## References


[1] Gong, C.; Li, L.; Li, Z. L.; Ji, H. W.; Stern, A.; Xia, Y.; Cao, T.; Bao, W.; Wang, C. Z.; Wang, Y. et al. Discovery of intrinsic ferromagnetism in two-dimensional van der Waals crystals. *Nature* **2017**, *546*, 265–269.

[2] Huang, B.; Clark, G.; Navarro-Moratalla, E.; Klein, D. R.; Cheng, R.; Seyler, K. L.; Zhong, D.; Schmidgall, E.; McGuire, M. A.; Cobden, D. H. et al. Layer-dependent ferromagnetism in a van der Waals crystal down to the monolayer limit. *Nature* **2017**, *546*, 270–273.

[3] Burch, K. S.; Mandrus, D.; Park, J. G. Magnetism in two-dimensional van der Waals materials. *Nature* **2018**, *563*, 47–52.

[4] Gong, C.; Zhang, X. Two-dimensional magnetic crystals and emergent heterostructure devices. *Science* **2019**, *363*, eaav4450.

[5] Gibertini, M.; Koperski, M.; Morpurgo, A. F.; Novoselov, K. S. Magnetic 2D materials and heterostructures. *Nat. Nanotechnol.* **2019**, *14*, 408–419.

[6] Bonilla, M.; Kolekar, S.; Ma, Y. J.; Diaz, H. C.; Kalappattil, V.; Das, R.; Eggers, T.; Gutierrez, H. R.; Phan, M. H.; Batzill, M. Strong room-temperature ferromagnetism in $VSe_2$ monolayers on van der Waals substrates. *Nat. Nanotechnol.* **2018**, *13*, 289–293.

[7] Nakano, M.; Wang, Y.; Yoshida, S.; Matsuoka, H.; Majima, Y.; Ikeda, K.; Hirata, Y.; Takeda, Y.; Wadati, H.; Kohama, Y. et al. Intrinsic 2D ferromagnetism in $V_5Se_8$ epitaxial thin films. *Nano Lett.* **2019**, *19*, 8806–8810.

[8] O'Hara, D. J.; Zhu, T. C.; Trout, A. H.; Ahmed, A. S.; Luo, Y. K.; Lee, C. H.; Brenner, M. R.; Rajan, S.; Gupta, J. A.; McComb, D. W. et al. Room temperature intrinsic ferromagnetism in epitaxial manganese selenide films in the monolayer limit. *Nano Lett.* **2018**, *18*, 3125–3131.

[9] Balan, A. P.; Radhakrishnan, S.; Woellner, C. F.; Sinha, S. K.; Deng, L. Z.; de los Reyes, C.; Rao, B. M.; Paulose, M.; Neupane, R.; Apte, A. et al. Exfoliation of a non-van der Waals material from iron ore hematite. *Nat. Nanotechnol.* **2018**, *13*, 602–609.

[10] Deng, Y. J.; Yu, Y. J.; Song, Y. C.; Zhang, J. Z.; Wang, N. Z.; Sun, Z. Y.; Yi, Y. F.; Wu, Y. Z.; Wu, S. W.; Zhu, J. Y. et al. Gate-tunable room-temperature ferromagnetism in two-dimensional $Fe_3GeTe_2$. *Nature* **2018**, *563*, 94–99.

[11] Tokmachev, A. M.; Averyanov, D. V.; Parfenov, O. E.; Taldenkov, A. N.; Karateev, I. A.; Sokolov, I. S.; Kondratev, O. A.; Storchak, V. G. Emerging two-dimensional ferromagnetism in silicene materials. *Nat. Commun.* **2018**, *9*, 1672.

[12] Tokmachev, A. M.; Averyanov, D. V.; Taldenkov, A. N.; Parfenov, O. E.; Karateev, I. A.; Sokolov, I. S.; Storchak, V. G. Lanthanide $f^7$ metalloxenes—A class of intrinsic 2D ferromagnets. *Mater. Horiz.* **2019**, *6*, 1488–1496.

[13] Sun, Z. Y.; Yi, Y. F.; Song, T. C.; Clark, G.; Huang, B.; Shan, Y. W.; Wu, S.; Huang, D.; Gao, C. L.; Chen, Z. H. et al. Giant nonreciprocal second-harmonic generation from antiferromagnetic bilayer $CrI_3$. *Nature* **2019**, *572*, 497–501.

[14] Thiel, L.; Wang, Z.; Tschudin, M. A.; Rohner, D.; Gutiérrez-Lezama, I.; Ubrig, N.; Gibertini, M.; Giannini, E.; Morpurgo, A. F.; Maletinsky, P. Probing magnetism in 2D materials at the nanoscale with single-spin microscopy. *Science* **2019**, *364*, 973–976.

[15] Niu, B.; Su, T.; Francisco, B. A.; Ghosh, S.; Kargar, F.; Huang, X.; Lohmann, M.; Li, J. X.; Xu, Y. D.; Taniguchi, T. et al. Coexistence of magnetic orders in two-dimensional magnet $CrI_3$. *Nano Lett.* **2020**, *20*, 553–558.

[16] Huang, B.; Clark, G.; Klein, D. R.; MacNeill, D.; Navarro-Moratalla, E.; Seyler, K. L.; Wilson, N.; McGuire, M. A.; Cobden, D. H.; Xiao, D. et al. Electrical control of 2D magnetism in bilayer $CrI_3$. *Nat. Nanotechnol.* **2018**, *13*, 544–548.

[17] Jiang, S. W.; Li, L. Z.; Wang, Z. F.; Mak, K. F.; Shan, J. Controlling magnetism in 2D $CrI_3$ by electrostatic doping. *Nat. Nanotechnol.* **2018**, *13*, 549–553.

[18] Song, T. C.; Fei, Z. Y.; Yankowitz, M.; Lin, Z.; Jiang, Q. N.; Hwangbo, K.; Zhang, Q.; Sun, B. S.; Taniguchi, T.; Watanabe, K. et al. Switching 2D magnetic states via pressure tuning of layer stacking. *Nat. Mater.* **2019**, *18*, 1298–1302.

[19] Klein, D. R.; MacNeill, D.; Lado, J. L.; Soriano, D.; Navarro-Moratalla, E.; Watanabe, K.; Taniguchi, T.; Manni, S.; Canfield, P.; Fernández-Rossier, J. et al. Probing magnetism in 2D van der Waals crystalline insulators via electron tunneling. *Science* **2018**, *360*, 1218–1222.

[20] Molle, A.; Goldberger, J.; Houssa, M.; Xu, Y.; Zhang, S. C.; Akinwande, D. Buckled two-dimensional Xene sheets. *Nat. Mater.* **2017**, *16*, 163–169.

[21] Mannix, A. J.; Kiraly, B.; Hersam, M. C.; Guisinger, N. P. Synthesis and chemistry of elemental 2D materials. *Nat. Rev. Chem.* **2017**, *1*, 0014.

[22] Tao, L.; Cinquanta, E.; Chiappe, D.; Grazianetti, C.; Fanciulli, M.; Dubey, M.; Molle, A.; Akinwande, D. Silicene field-effect transistors operating at room temperature. *Nat. Nanotechnol.* **2015**, *10*, 227–231.

[23] Wang, Y. Y.; Zheng, J. X.; Ni, Z. Y.; Fei, R. X.; Liu, Q. H.; Quhe, R.; Xu, C. Y.; Zhou, J.; Gao, Z. X.; Lu, J. Half-metallic silicene and germanene nanoribbons: Towards high-performance spintronics device. *Nano* **2012**, *7*, 1250037.

[24] Zhao, J. J.; Liu, H. S.; Yu, Z. M.; Quhe, R.; Zhou, S.; Wang, Y. Y.; Liu, C. C.; Zhong, H. X.; Han, N. N.; Lu, J. et al. Rise of silicene: A competitive 2D material. *Prog. Mater. Sci.* **2016**, *83*, 24–151.

[25] Tokmachev, A. M.; Averyanov, D. V.; Karateev, I. A.; Parfenov, O. E.; Kondratev, O. A.; Taldenkov, A. N.; Storchak, V. G. Engineering of magnetically intercalated silicene compound: An overlooked polymorph of $EuSi_2$. *Adv. Funct. Mater.* **2017**, *27*, 1606603.

[26] Parfenov, O. E.; Averyanov, D. V.; Tokmachev, A. M.; Sokolov, I. S.; Karateev, I. A.; Taldenkov, A. N.; Storchak, V. G. High-mobility carriers in germanene derivatives. *Adv. Funct. Mater.* **2020**, *30*, 1910643.

[27] Parfenov, O. E.; Tokmachev, A. M.; Averyanov, D. V.; Karateev, I. A.; Sokolov, I. S.; Taldenkov, A. N.; Storchak, V. G. Layer-controlled laws of electron transport in two-dimensional ferromagnets. *Mater. Today* **2019**, *29*, 20–25.

[28] Zhai, X. C.; Wen, R.; Zhou, X. F.; Chen, W.; Yan, W.; Gong, L. Y.; Pu, Y.; Li, X. A. Valley-mediated and electrically switched bipolar-unipolar transition of the spin-diode effect in heavy group-IV monolayers. *Phys. Rev. Appl.* **2019**, *11*, 064047.

[29] Feng, J. G.; Biswas, D.; Rajan, A.; Watson, M. D.; Mazzola, F.; Clark, O. J.; Underwood, K.; Marković, I.; McLaren, M.; Hunter, A. et al. Electronic structure and enhanced charge-density wave order of monolayer $VSe_2$. *Nano Lett.* **2018**, *18*, 4493–4499.

[30] Wong, P. K. J.; Zhang, W.; Bussolotti, F.; Yin, X. M.; Herng, T. S.; Zhang, L.; Huang, Y. L.; Vinai, G.; Krishnamurthi, S.; Bukhvalov, D. W. et al. Evidence of spin frustration in a vanadium diselenide monolayer magnet. *Adv. Mater.* **2019**, *31*, 1901185.

[31] Averyanov, D. V.; Sadofyev, Y. G.; Tokmachev, A. M.; Primenko, A. E.; Likhachev, I. A.; Storchak, V. G. Direct epitaxial integration of the ferromagnetic semiconductor EuO with silicon for spintronic applications. *ACS Appl. Mater. Interfaces* **2015**, *7*, 6146–6152.

[32] Nigh, H. E.; Legvold, S.; Spedding, F. H. Magnetization and electrical resistivity of gadolinium single crystals. *Phys. Rev.* **1963**, *132*, 1092–1097.

[33] Sanna, S.; Dues, C.; Schmidt, W. G.; Timmer, F.; Wollschläger, J.; Franz, M.; Appelfeller, S.; Dähne, M. Rare-earth silicide thin films on the Si(111) surface. *Phys. Rev. B* **2016**, *93*, 195407.

[34] Yu, W.; Li, J.; Herng, T. S.; Wang, Z. S.; Zhao, X. X.; Chi, X.; Fu, W.; Abdelwahab, I.; Zhou, J.; Dan, J. D. et al. Chemically exfoliated $VSe_2$ monolayers with room-temperature ferromagnetism. *Adv. Mater.* **2019**, *31*, 1903779.

[35] Mak, K. F.; Shan, J.; Ralph, D. C. Probing and controlling magnetic states in 2D layered magnetic materials. *Nat. Rev. Phys.* **2019**, *1*, 646–661.

[36] Frisk, A.; Duffy, L. B.; Zhang, S. L.; van der Laan, G.; Hesjedal, T. Magnetic X-ray spectroscopy of two-dimensional $CrI_3$ layers. *Mater. Lett.* **2018**, *232*, 5–7.

[37] Li, Q.; Yang, M. M.; Gong, C.; Chopdekar, R. V.; N'Diaye, A. T.; Turner, J.; Chen, G.; Scholl, A.; Shafer, P.; Arenholz, E. et al. Patterning-induced ferromagnetism of $Fe_3GeTe_2$ van der Waals materials beyond room temperature. *Nano Lett.* **2018**, *18*, 5974–5980.

[38] Park, S. Y.; Kim, D. S.; Liu, Y.; Hwang, J.; Kim, Y.; Kim, W.; Kim, J. Y.; Petrovic, C.; Hwang, C.; Mo, S. K. et al. Controlling the magnetic anisotropy of the van der Waals ferromagnet $Fe_3GeTe_2$

through hole doping. *Nano Lett*. **2020**, *20*, 95–100.
[39] Girovsky, J.; Nowakowski, J.; Ali, M. E.; Baljozovic, M.; Rossmann, H. R.; Nijs, T.; Aeby, E. A.; Nowakowska, S.; Siewert, D.; Srivastava, G. et al. Long-range ferrimagnetic order in a two-dimensional supramolecular Kondo lattice. *Nat. Commun*. **2017**, *8*, 15388.
[40] Schulz, S.; Nechaev, I. A.; Güttler, M.; Poelchen, G.; Generalov, A.; Danzenbächer, S.; Chikina, A.; Seiro, S.; Kliemt, K.; Vyazovskaya, A. Y. et al. Emerging 2D-ferromagnetism and strong spin-orbit coupling at the surface of valence-fluctuating $EuIr_2Si_2$. *npj Quantum Mater*. **2019**, *4*, 26.
[41] Guo, G. Y. Interpretation of X-ray circular dichroism: Multiple-scattering theory approach. *Phys. Rev. B* **1998**, *57*, 10295–10298.
[42] Li, Y. F.; Zhang, K. C.; Liu, Y. Structural, magnetic and topological properties in rare-earth-adsorbed silicene system. *J. Magn. Magn. Mater*. **2019**, *492*, 165606.
[43] Antoniak, C.; Herper, H. C.; Zhang, Y. N.; Warland, A.; Kachel, T.; Stromberg, F.; Krumme, B.; Weis, C.; Fauth, K.; Keune, W. et al. Induced magnetism on silicon in $Fe_3Si$ quasi-Heusler compound. *Phys. Rev. B* **2012**, *85*, 214432.
[44] Taupin, M.; Sanchez, J. P.; Brison, J. P.; Aoki, D.; Lapertot, G.; Wilhelm, F.; Rogalev, A. Microscopic magnetic properties of the ferromagnetic superconductor UCoGe reviewed by X-ray magnetic circular dichroism. *Phys. Rev. B* **2015**, *92*, 035124.
[45] Thole, B. T.; Carra, P.; Sette, F.; van der Laan, G. X-ray circular dichroism as a probe of orbital magnetization. *Phys. Rev. Lett*. **1992**, *68*, 1943–1946.
[46] Carra, P.; Thole, B. T.; Altarelli, M.; Wang, X. D. X-ray circular dichroism and local magnetic fields. *Phys. Rev. Lett*. **1993**, *70*, 694–697.
[47] van der Laan, G.; Thole, B. T. X-ray-absorption sum rules in *jj*-coupled operators and ground- state moments of actinide ions. *Phys. Rev. B* **1996**, *53*, 14458–14469.
[48] Leuenberger, F.; Parge, A.; Felsch, W.; Fauth, K.; Hessler, M. GdN thin films: Bulk and local electronic and magnetic properties. *Phys. Rev. B* **2005**, *72*, 014427.
[49] Averyanov, D. V.; Parfenov, O. E.; Tokmachev, A. M.; Karateev, I. A.; Kondratev, O. A.; Taldenkov, A. N.; Platunov, M. S.; Wilhelm, F.; Rogalev, A.; Storchak, V. G. Fine structure of metal-insulator transition in EuO resolved by doping engineering. *Nanotechnology* **2018**, *29*, 195706.
[50] Averyanov, D. V.; Tokmachev, A. M.; Parfenov, O. E.; Karateev, I. A.; Sokolov, I. S.; Taldenkov, A. N.; Platunov, M. S.; Wilhelm, F.; Rogalev, A.; Storchak, V. G. Probing proximity effects in the ferromagnetic semiconductor EuO. *Appl. Surf. Sci*. **2019**, *488*, 107–114.
[51] Bauer, J.; Pascher, H. Diluted magnetic IV-VI compounds. In *Diluted Magnetic Semiconductors*. Jain, M., Ed.; World Scientific: Singapore, 1991; pp 339–407.
[52] Torelli, D.; Thygesen, K. S.; Olsen, T. High throughput computational screening for 2D ferromagnetic materials: The critical role of anisotropy and local correlations. *2D Mater*. **2019**, *6*, 045018.
[53] Kim, K.; Lim, S. Y.; Lee, J. U.; Lee, S.; Kim, T. Y.; Park, K.; Jeon, G. S.; Park, C. H.; Park, J. G.; Cheong, H. Suppression of magnetic ordering in XXZ-type antiferromagnetic monolayer $NiPS_3$. *Nat. Commun*. **2019**, *10*, 345.
[54] Liao, Z. Q.; Standke, Y.; Gluch, J.; Brázda, P.; Kopeček, J.; Klementová, M.; Palatinus, L.; Zschech, E. Cleaving silicene-terminated calcium disilicide in the transmission electron microscope. *Nanotechnology* **2020**, *31*, 095702.
[55] Appelfeller, S.; Franz, M.; Freter, L.; Hassenstein, C.; Jirschik, H. F.; Dähne, M. Growth and characterization of Tb silicide nanostructures on Si(hhk) substrates. *Phys. Rev. Mater*. **2019**, *3*, 126002.
[56] Sokolov, I. S; Averyanov, D. V.; Parfenov, O. E.; Karateev, I. A.; Taldenkov, A. N.; Tokmachev, A. M.; Storchak, V. G. 2D ferromagnetism in europium/graphene bilayers. *Mater. Horiz*. **2020**, *7*, 1372–1378.
[57] Barla, A.; Nicolás, J.; Cocco, D.; Valvidares, S. M.; Herrero-Martín, J.; Gargiani, P.; Moldes, J.; Ruget, C.; Pellegrin, E.; Ferrer, S. Design and performance of BOREAS, the beamline for resonant X-ray absorption and scattering experiments at the ALBA synchrotron light source. *J. Synchrotron Rad*. **2016**, *23*, 1507–1517.
[58] Ohresser, P.; Otero, E.; Choueikani, F.; Chen, K.; Stanescu, S.; Deschamps, F.; Moreno, T.; Polack, F.; Lagarde, B.; Daguerre, J. P. et al. DEIMOS: A beamline dedicated to dichroism measurements in the 350–2500 eV energy range. *Rev. Sci. Instrum*. **2014**, *85*, 013106.